OpenFOAM® Journal

Volume 5 [Full Papers], Pages 131–147
ISSN: 2753-8168

Prediction of Crossflow Transition using γ Transition Model Coupled with Reynolds Stress Transport Turbulence Model

Naina Pisharoti* and Stefano Brizzolara

Department of Aerospace and Ocean Engineering, Virginia Tech, Blacksburg, Virginia, USA.
Email address: pnaina@vt.edu

DOI: https://doi.org/10.51560/ofj.v5.130
Results with version(s): OpenFOAM® v2006
Repository: https://github.com/nainapisharoti/SSG-LRR-omega-gamma

Abstract. This study presents an enhanced second-order closure transition model, SSG/LRR-ω-γ, incorporating crossflow transition effects for improved prediction of laminar–turbulent transition in three-dimensional boundary layers. The original formulation couples the SSG/LRR-ω Reynolds stress model with Menter's one-equation γ transition model to address streamwise instabilities. To extend its capabilities, a local helicity-based criterion is introduced to account for crossflow-induced transition. The modified model is assessed using two benchmark configurations: the NLF(2)-0415 infinite swept wing and the DLR 6:1 prolate spheroid, across a range of operating conditions. A grid sensitivity analysis is also performed to ensure numerical robustness. Results demonstrate that the crossflow model accurately captures crossflow-induced transition and provides improved agreement with experimental data compared to the original streamwise-only formulation.

1. Introduction

Transition from laminar to turbulent flow is a phenomenon commonly observed in many wall-bounded aerodynamic and hydrodynamic scenarios. This process holds particular significance in a variety of research areas and practical applications that operate at low to moderate Reynolds numbers. For example, optimizing the design of autonomous underwater vehicles (AUVs) [1, 2], implementing laminar flow control to reduce drag in aircraft [3, 4], refining propeller designs for marine vessels [5], and assessing the aerodynamic and aeroacoustic performance of unmanned aerial vehicles (UAVs) [6, 7] are all actively pursued fields where understanding and managing flow transition is crucial. This boundary layer phenomenon directly impacts surface pressure and shear distribution, which in turn influences the forces and moments generated by these vehicles or components.

Flow transition is influenced by factors such as Mach number, Reynolds number, body shape, and surface properties [8]. Predicting this transition is challenging due to the interplay of linear and nonlinear instabilities, which result in various modes including natural, bypass, separation-induced, and crossflow transition. This complexity has made accurate modeling a persistent challenge for the CFD community. Historically, transition models have primarily focused on predicting streamwise transition mechanisms such as natural, separation-induced, or bypass transition [9–12], with later extensions addressing crossflow transitions [13–18]. Natural transition occurs when a body encounters low freestream turbulence (typically less than 1%), and the laminar boundary layer begins to destabilize due to acoustic or viscous disturbances. In 1947, Schubauer and Skramstad [19] experimentally confirmed the existence of two-dimensional Tollmien–Schlichting (TS) waves, which arise from viscous instabilities in a laminar boundary layer. These instabilities grow at a gradual pace and eventually transition to turbulent flow. In contrast, crossflow transition occurs in highly three-dimensional flows where velocity components introduce a strong yaw effect and favorable pressure gradients, potentially triggering transition earlier than predicted by the TS mechanism. This premature triggering due to crossflow instability is challenging to model due to its inherently three-dimensional nature. In practical applications like underwater vehicles,

* Corresponding author

Received: 14 February 2024, Accepted: 16 June 2025, Published: 8 September 2025

low-speed airships, and aircrafts, complex three-dimensional boundary layer flows give rise to significant crossflow velocities, making accurate modeling of crossflow-induced transition essential for reliable performance prediction.

One of the most widely used transition models is the γ-$Re_{\theta t}$ model, which incorporates the local correlation-based transport model (LCTM) [9]. This model uses transport equations for the intermittency factor (γ), which determines whether the flow is turbulent, and the transition momentum thickness Reynolds number ($Re_{\theta t}$) to model streamwise transition. Several efforts have aimed at extending this model to account for crossflow transition effects [13–16]. A semi-local approach introduced by Grabe *et al.* [13] and Medida *et al.* [14] showed promising results but was dependent on geometry type and required local reference frame information. To address these limitations, Langtry developed a new crossflow transition model based on local helicity criteria [15, 20], recognizing helicity as a significant factor in crossflow transition. This model also included transition due to roughness effects. Grabe *et al.* [16] compared two models with different crossflow transition criteria: the first, referred to as 'local-C1,' was based on Arnal's C1 transition criterion [21], while the second model used a helicity-based approach. They concluded that the helicity-based model is more broadly applicable across a range of geometries, whereas the C1 approach is more effective for wing-like geometries. All the models discussed so far couple the γ-$Re_{\theta t}$ transition model with the k-ω SST model. Recent efforts have also focused on integrating the transition model with the Spalart-Allmaras fully turbulent model framework [22].

The γ-$Re_{\theta t}$ transition model has certain drawbacks, such as its complex formulation and reliance on free-stream quantities like turbulence intensity to calculate $Re_{\theta t}$, which limits its applicability to stationary walls. To address these issues, Menter *et al.* [10] introduced a modified single-equation model that removed the dependency on $Re_{\theta t}$, simplifying the formulation and ensuring Galilean invariance. This model was later extended to include crossflow effects by Pillai *et al.* [17] and implemented on the commercial CFD software StarCCM+. The extended model incorporated a helicity-based formulation to address crossflow transition and included surface roughness effects. It was validated with experiments on a sickle wing, a prolate spheroid, and the Onera-M6 wing, demonstrating good agreement with experimental data.

To advance transition modeling with higher-order approaches, Nie *et al.* introduced a Reynolds stress transport (RST)-based transition model, coupling the fully turbulent SSG/LRR-ω model with the γ-$Re_{\theta t}$ transition model [11]. RST-based models are known for their greater accuracy in flows with strong streamline curvature, as they do not rely on the linear Boussinesq approximation to compute turbulent stresses. By modeling the anisotropic components of the Reynolds stress, they offer better accuracy than linear eddy viscosity models. Initially developed for streamwise transition, this model was later extended to incorporate crossflow transition effects [18]. However, because it employs the γ-$Re_{\theta t}$ model for transition prediction, it inherits its drawbacks that were discussed earlier.

To combine the advantages of a higher-order RST-based model with a simplified transition formulation, Pisharoti *et al.* [12] introduced the SSG/LRR-ω-γ transition model, which couples the SSG/LRR-ω turbulent model with a single transport equation for intermittency (γ). This model uses simplified correlations with tunable coefficients that rely only on local quantities within the boundary layer. It was validated against various benchmark cases, demonstrating accurate predictions for different streamwise transition mechanisms [6, 12, 23]. However, the model currently lacks the capability to handle crossflow transition.

This paper focuses on incorporating crossflow transition into the novel SSG/LRR-ω-γ model framework. The current formulation uses the local helicity-based criterion, which has proven effective in capturing crossflow effects, as discussed earlier. A summary of the original streamwise model, SSG/LRR-ω-γ, and its extension to account for crossflow - referred to hereafter as 'SSG/LRR-ω-γ-CF' - is provided in Section 2. The model is validated using two benchmark test cases known for exhibiting crossflow transition: the NLF (2)-0415 infinite swept wing at various Reynolds numbers [3] and the DLR 6:1 prolate spheroid at different inclinations [24]. Additionally, a study examining the influence of the computational grid and numerical scheme on model performance is presented for each test case. All simulations were performed using OpenFOAM-v2006. Through this work, the authors aim to enhance the OpenFOAM turbulence modeling library, which currently lacks higher-order streamwise transition models and has a notable absence of crossflow transition models.

2. Formulation of SSG/LRR-ω-γ-CF Transition Model

2.1. SSG/LRR-ω-γ Model Formulation for Streamwise Transition. Pisharoti *et al.* [12] initially introduced the SSG/LRR-ω-γ model to capture various transition mechanisms, including natural, bypass, separation, and wake-induced transitions, and validated it thoroughly within OpenFOAM-v2006. This

paper builds on that foundation by extending the model to incorporate crossflow transition. To provide context, this section briefly reviews the streamwise transition model before introducing the modifications for crossflow effects. The complete set of model equations is presented in Appendix A, and further details on validation can be found in the work by Pisharoti *et al.* [12].

The framework for the SSG/LRR-ω-γ model is given by

$$\frac{\partial \rho R_{ij}}{\partial t} + \frac{\partial (\rho U_k R_{ij})}{\partial x_k} = \rho \tilde{P}_{ij} + \rho \tilde{\Pi}_{ij} - \rho \tilde{\epsilon}_{ij} + \rho D_{ij}, \tag{1}$$

$$\begin{aligned} \frac{\partial (\rho\omega)}{\partial t} + \frac{\partial (\rho U_k \omega)}{\partial x_k} = \rho \tilde{P}_\omega - \beta \rho \omega^2 + \frac{\partial}{\partial x_k}\left[\left(\mu + \sigma_\omega \frac{\rho k}{\omega}\right)\frac{\partial \omega}{\partial x_k}\right] \\ + \sigma_d \frac{\rho}{\omega} max\left(\frac{\partial k}{\partial x_j}\frac{\partial \omega}{\partial x_j}, 0\right), \end{aligned} \tag{2}$$

$$\frac{\partial (\rho\gamma)}{\partial t} + \frac{\partial (\rho U_j \gamma)}{\partial x_j} = P_\gamma - E_\gamma + \frac{\partial}{\partial x_j}\left[\left(\mu + \frac{\mu_t}{\sigma_\gamma}\right)\frac{\partial \gamma}{\partial x_j}\right]. \tag{3}$$

Equation (1) represents the Reynolds stress transport, modeling all six components of the Reynolds stress. The coefficients in the Reynolds stress transport equation are a blend of the SSG and LRR models, combined through a blending function similar to that used in the SST-based γ transition model [10]. The system of equations is then closed using the length-scale determining equation (ω), given in Eqn. (2) [25].

Equation (3) represents the intermittency transport, where P_γ denotes the production of intermittency and E_γ stands for its dissipation. This equation governs the modeling of transition. It is coupled with the Reynolds stress transport equation by scaling the production (P_{ij}), dissipation (ϵ_{ij}) and pressure-strain term (Π_{ij}) with intermittency (γ), as

$$\tilde{P}_{ij} = \gamma P_{ij} \quad , \quad \tilde{\epsilon}_{ij} = \max(\gamma, 0.1)\epsilon_{ij} \quad , \quad \tilde{\Pi}_{ij} = \gamma \Pi_{ij}. \tag{4}$$

It follows the coupling approach used in the SST-based γ transition model introduced by Menter *et al.* [10]. In laminar regions, where intermittency values are low ($\gamma \approx 0$), scaling the production term with γ ensures minimal turbulent Reynolds stresses. The coupling mechanism allows for the destruction of turbulence to exceed its production, while low levels of the pressure-strain term prevent the redistribution of turbulent stresses. Conversely, in turbulent regions, where intermittency reaches 1, the model regains its turbulent behavior.

In RST-based transition models, as the Reynolds stress tensor (R_{ij}) goes down to near zero values in the fully laminar regions, the turbulence production term becomes negligible. Since the production of the specific dissipation rate is directly proportional to the trace of turbulence production (P_{kk}), as

$$P_{\omega_{RST}} = \frac{\alpha_\omega \omega}{k}\frac{\rho P_{kk}}{2}, \tag{5}$$

the dissipation also drops to really low levels. This reduction leads to a faster turbulence growth rate and premature transition. However, this issue does not arise in SST-based transition models, where the dissipation terms are a function of the mean strain rate (S), as

$$P_{\omega_{SST}} = \frac{\alpha_\omega}{\nu_t}\left(-\rho R_{ik}\frac{\partial U_i}{\partial x_k}\right) = \alpha_\omega \rho S^2, \tag{6}$$

which stems directly from the Boussinesq approximation $R_{ij} = -\,(\,2\nu_t S_{ij} - 2k\delta_{ij}/3\,)$, where ν_T is the turbulent kinematic viscosity.

Therefore, a modification was introduced to the dissipation production as

$$\tilde{P}_\omega \;=\; (1 \;-\; C_{lam})P_{\omega_{SST}} \;+\; C_{lam}P_{\omega_{RST}}, \tag{7}$$

where

$$C_{lam} \;=\; \begin{cases} 0 & \text{if } c_\omega \;>\; \gamma \\ \frac{\gamma - c_\omega}{1 - c_\omega} & \text{if } c_\omega \;<\; \gamma \end{cases} \text{ and } c_\omega \;=\; \left(\exp\left(-\left(\frac{420}{Re_{\theta c} + C_{Re}}\right)^4\right)\right)^2, \tag{8}$$

$$C_{Re} = 500.$$

Here, C_{lam} is a blending function that equals 0 in laminar regions which activates the SST-based formulation of dissipation production and equals 1 in turbulent regions, which activates the original formulation of RST-based dissipation production. The term C_{Re} is a model constant and is accessible to the user for any changes. The term $Re_{\theta c}$ represents the critical Reynolds number and is a key parameter in defining the streamwise transition criteria, which will be discussed in the following section. This modified hybrid formulation helps in predicting transition for cases with high free-stream turbulence by improving ω prediction in fully laminar regions.

Additionally, in cases with low levels of free-stream turbulence, it has been observed that the SSG/LRR-ω-γ model takes longer to generate turbulence within the boundary layer, even though the transition is triggered at the correct location [10, 12]. Therefore, an auxiliary turbulence production term, P_{ij}^{lim} was introduced and added to the original Reynolds stress production, as

$$\tilde{P}_{ij} = \gamma P_{ij} + P_{ij}^{lim}, \tag{9}$$

where

$$P_{ij}^{lim} = 5C_k max(\gamma - 0.2, 0)(1-\gamma)F_{on}^{lim} max(3C_{SEP}\nu - \nu_T, 0)\frac{\omega}{k}P_{kk}\delta_{ij}. \tag{10}$$

It aids in generating additional turbulence when transition is driven by laminar separation, or by TS wave growth. The term is activated when transition is triggered and deactivated once the flow becomes fully turbulent. The onset term F_{on}^{lim} is given by

$$F_{lim}^{on} = \min\left(\max\left(\frac{Re_\nu}{2.2Re_{\theta_C}^{lim}} - 1, 0\right), 3\right) \quad , \quad Re_{\theta_c}^{lim} = 1100. \tag{11}$$

The constant C_k controls the magnitude of supplementary turbulence production and is equal to 1. The constant C_{SEP}, which is set to 1, is responsible to deactivate the supplementary term when the magnitude of turbulent viscosity (ν_T) goes higher than three times the kinematic viscosity (ν). The term $Re_\nu = \frac{\rho y^2 S}{\mu}$ stands for vorticity Reynolds number, where S is the magnitude of the mean strain rate tensor and y is the distance from the wall.

2.2. **Extension for Crossflow Transition.** To incorporate effects of crossflow transition, the only term that needs to be altered from the original SSG/LRR-ω-γ formulation is the production of intermittency in Eqn. (3). The γ-production term is modified by adding a crossflow production term as

$$\rho P_\gamma = \rho P_{\gamma,sw} + \rho P_{\gamma,cf}. \tag{12}$$

The subscript sw represents stream-wise terms and cf represents crossflow terms. The stream-wise intermittency production is unchanged from the original SSG/LRR-ω-γ model and is given by

$$\rho P_{\gamma,sw} = F_{length,sw}\rho S\gamma(1-\gamma)F_{onset,sw}. \tag{13}$$

Here, $F_{length,sw}$ represents the length of the transition region and is set to 100. The term '(1 - γ)' is used to ensure that the intermittency value does not exceed 1 and $F_{onset,sw}$ controls the transition onset location and is defined as

$$\begin{aligned} F_{onset1,sw} = \frac{Re_\nu}{2.2Re_{\theta c}}, \quad F_{onset2,sw} &= \min(F_{onset1,sw}, 2.0), \\ F_{onset3,sw} &= \max\left(1 - \left(\frac{R_T}{3.5}\right)^3, 0\right), \\ F_{onset,sw} &= \max(F_{onset2,sw} - F_{onset3,sw}, 0). \end{aligned} \tag{14}$$

The critical Reynolds number, $Re_{\theta c}$, depends on turbulence intensity and pressure gradient, which are modeled using fully local variables as described by Menter *et al.* [10]. Since the formulation relies only on local variables and is not influenced by freestream conditions, it is Galilean invariant. The term R_T represents the viscosity ratio ($\frac{\rho k}{\mu\omega} = \frac{\nu_t}{\nu}$).

Similar to the stream-wise production, the crossflow production is given by

$$\rho P_{\gamma,cf} = F_{length,cf}\rho S\gamma(1-\gamma)F_{onset,cf}. \tag{15}$$

The model correlations in this expression are based on the local helicity approach introduced by Grabe *et al.* [16]. In this model, $F_{length,cf}$ regulates the magnitude of the production term responsible for crossflow transition. A calibration study, conducted using the NLF(2)-0415 swept wing [3] and the DLR 6:1 spheroid [24], determined an optimal value of 5, aligning with the formulation proposed by Grabe *et al.* [16]. It was observed that higher values of this constant result in a substantial increase in intermittency production, leading to an earlier onset of transition.

The term $F_{onset,cf}$ is responsible for triggering the transition mechanism. The criterion for determining the onset location of crossflow transition is based on helicity (He), defined as the dot product of the local velocity vector (u_k), i.e., the velocity at each point in the computational grid, and the vorticity vector, as

$$He = |u_k \cdot (\nabla \times u_k)| \quad , \quad Re_{He} = \frac{y^2}{\nu}\frac{He}{|u_k|} \tag{16}$$

$$F_{onset1,cf} = \frac{Re_{He}}{Re_{He,C}} \quad , \quad F_{onset2,cf} = \min(F_{onset1,cf}, 2.0)$$
$$F_{onset3,cf} = \max\left(1 - \left(\frac{R_T}{3.5}\right)^3, 0\right) \tag{17}$$
$$F_{onset,cf} = \max(F_{onset2,cf} - F_{onset3,cf}, 0)$$

The helicity is an indication of how aligned the two vectors are. It is non-dimensionalized to yield the local helicity Reynolds number, Re_{He}. This quantity effectively detects crossflow instabilities, as it depends on crossflow velocity gradients [16, 18]. It plays a role similar to the vorticity Reynolds number, Re_ν, which detects the onset of instabilities in streamwise transition and is based on streamwise velocity gradients. A drawback of using quantities like helicity is that, because it depends on both velocity and vorticity, which change under a Galilean transformation, the model formulation becomes sensitive to the reference frame. Consequently, extending the model to account for crossflow transition leads to a loss of Galilean invariance. This is largely not a concern in most practical cases. However, the presence of multiple reference frames, such as in rotating machinery simulations, can lead to solutions that depend on the chosen frame, which is unphysical. It can, for example, lead to incorrect prediction of transition and separation locations.

The correlation for $Re_{He,C}$ is given as a function of shape factor, H, as

$$Re_{He,C} = 0.55 \max(-456.83H + 1337.2, 150.0). \tag{18}$$

The shape factor is further calculated using a correlation presented by Pillai *et al.* [17] and given by

$$H(\lambda) = 2 + 4.14k - 83.5k^2 + 854k^3 - 3337k^4 + 4576k^5, \tag{19}$$

where, $k = 0.25 - \lambda$. It is modeled as a function of the local pressure gradient parameter, λ, which is readily available from the γ transition model [10, 12]. In earlier implementations, the correlation introduced by Cliquet *et al.* [26] was used. However, it was observed that for cases with significant crossflow transition, the correlation by Pillai *et al.* [17] demonstrated better performance.

3. **Validation Cases**

The current crossflow transition model was validated using two benchmark cases; the NLF (2)-0415 swept wing and the DLR 6:1 prolate spheroid. A grid sensitivity study was conducted for both cases. Additionally, both cases were examined under different operating conditions and compared with the streamwise transition model. All analyses were performed using grids generated with *snappyHexMesh*.

The boundary conditions were calculated according to the method specified for the SSG/LRR-ω model in the NASA turbulence modeling repository [27]. At far-field boundaries, isotropic turbulence is assumed. Freestream Reynolds stress ($\tilde{R}_{ij\infty}$) and dissipation rate (ω_∞) are given as

$$\tilde{R}_{ij\infty} = \frac{2}{3}\tilde{k}_\infty \partial_{ij} \quad , \quad \omega_\infty = \frac{\tilde{k}_\infty}{\nu_{t\infty}}. \tag{20}$$

Here, $\tilde{k}_\infty$ is calculated using the freestream turbulence intensity as

$$\tilde{k}_\infty = \frac{3}{2} T u_\infty^2 U_\infty^2. \tag{21}$$

At the wall, the no-slip condition is assigned. The Reynolds stress tensor is set to a value of 0. The specific dissipation rate is defined as

$$\omega_{wall} = 10\frac{6\nu_{wall}}{0.075y^2}. \tag{22}$$

To ensure numerical stability for the RST-based model, all simulations were carried out using the unsteady solver *pimpleFoam*, with suitably chosen under-relaxation settings. The Courant number (CFL) was kept below 5 throughout the simulation. Initially, low under-relaxation factors were applied and gradually increased as the solution progressed to promote convergence and improve overall accuracy. A strict convergence criteria was enforced by setting the solution tolerances to the order of 10^{-7} for velocity and all turbulent quantities, while a tolerance of 10^{-4} was applied for pressure. The numerical schemes used for the analyses were the second-order *Crank-Nicolson* time integration scheme and *Gauss linearUpwind* spatial discretization. It is important to note that, for the stability of the current model, the divergence scheme for the Reynolds stress tensor was set to the *Gauss upwind* scheme. Gradient limiters were applied to all turbulent quantities. To fine-tune the *Crank-Nicolson* scheme coefficient, an initial value of 0.4 was used, which was gradually increased to 0.9 as the solution stabilized.

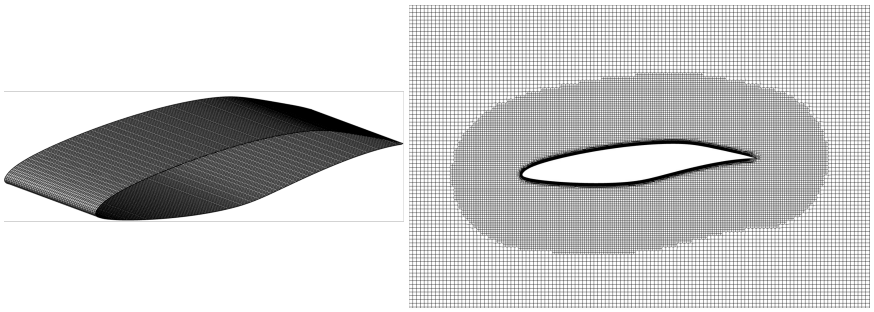

Figure 1. Near-body grid for the NLF (2)-0415 infinite swept wing

3.1. **NLF (2)-0415 Infinite Swept Wing.** The first test case considered in this study is the NLF (2)-0415 infinite swept wing, which has a 45° sweep. The experimental data for this case were obtained from tests conducted at the Arizona State University Unsteady Wind Tunnel [3]. In these experiments, hot wire measurements were used to investigate crossflow instabilities and transition along the wing surface at different angles of attack. For the current study, the test case at $\alpha = -4°$ was selected.

The computational domain was designed with the inlet located 10 chord lengths ($10c$) upstream of the leading edge and the outlet 15 chord lengths ($15c$) downstream of the trailing edge to avoid any influence from the boundaries. A periodic boundary condition (*cyclic* in OpenFOAM) was imposed on either side of the wing with a span of 0.3 chord lengths ($0.3c$). The top and bottom boundaries were placed 5 chord lengths ($5c$) from the wing, respectively, and were assigned a slip wall boundary condition. The right side of Fig. 1 shows the computational grid in the near-wall region of the wing. To achieve a perfect face and point match for the cyclic boundaries, a two-dimensional grid for the NLF(2)-0415 airfoil was initially generated and then extruded in the span-wise direction. The sweep angle was taken into account by setting the velocity vector at a 45° angle in the x-z (horizontal) plane. The initial conditions were set with the free-stream turbulence below 0.09% and the viscosity ratio (ν_t/ν) equal to 1. Intermittency (γ) was initialized at a value of 1 throughout the entire domain.

3.1.1. ***Grid Sensitivity Study.*** The grid sensitivity study for the swept wing was conducted using five different grids, with each grid progressively having finer near-body resolution. Since the focus of the current study is to capture boundary layer effects, emphasis has been placed on surface and near-wall grid parameters. Table 1 shows the grid parameters for each mesh, where Δx_{body} is the surface spacing on the swept wing, $y^+(1)$ determines the spacing of the first layer off the wall, and prism layers indicate the number of grid points in the wall-normal direction to resolve the boundary layer. To maintain a good aspect ratio on the wing surface, the x (chord-wise) and z (span-wise) directions have the same surface spacing Δx_{body}. The crossflow as well as the streamwise models were considered for the grid sensitivity study.

Table 1. Mesh parameters for grid-independence study on the NLF(2)-0415 swept wing at $Re = 3.73 \times 10^6$ and $\alpha = -4°$

	Coarse	**Medium**	**Fine**	**Finer**	**Finest**
Δx_{body}	9.5 mm	7.2 mm	4.8 mm	4.0 mm	3.0 mm
$y^+(1)$	1.2	1	0.8	0.55	0.4
Prism Layers	30	40	60	75	85
Total No. of Cells	8.3×10^5	2.7×10^6	5.3×10^6	11.1×10^6	20.6×10^6

Figure 2(a) shows the distribution of the skin-friction coefficient (C_f) along the suction side of the swept wing, as predicted by the crossflow model. The skin-friction coefficient is calculated by non-dimensionalizing the magnitude of wall-shear stress with the dynamic pressure ($1/2\rho U_\infty^2$). The *Coarse* mesh fails to predict any transition, instead showing a fully turbulent profile. Transition onset is observed with the *Medium* mesh, and the transition location shifts downstream as mesh resolution increases. The transition onset location is identified as the point where a sudden rise in the skin-friction distribution occurs, marked in red for each mesh in the plot. For reference, the experimentally measured transition onset location is also indicated. The predicted onset location seems to move closer to the previous grid's prediction with progressively finer grids. Figure 2(b) illustrates grid sensitivity trends for the streamwise transition model. Similar to the crossflow case, the *Coarse* grid displays fully turbulent

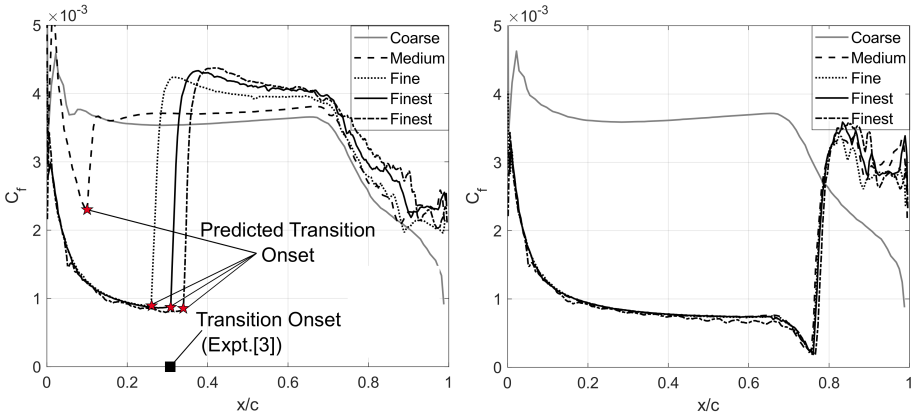

Figure 2. Grid Sensitivity Study conducted on the (a) SSG/LRR-ω-γ-CF and (b) SSG/LRR-ω-γ models for the NLF(2)-0415 airfoil

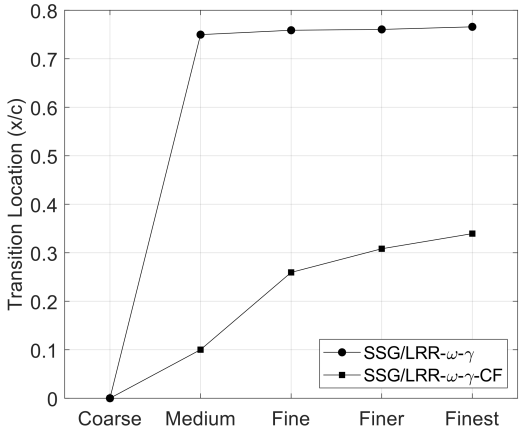

Figure 3. Grid convergence of transition onset location predicted by the SSG/LRR-ω-γ and the SSG/LRR-ω-γ-CF models

behavior, while transition is observed starting from the *Medium* grid. However, in this case, the transition onset occurs much farther downstream compared to both the experimental value and the crossflow model. Nevertheless, the grids seem to converge more effectively in this case than in the crossflow model.

Figure 3 illustrates the convergence of transition onset along the chord, as predicted by both models. The *Coarse* grid is assigned a chord-wise location of 0, since it is fully turbulent. The streamwise transition model shows rapid convergence beyond the *Medium* mesh, with minimal variation in the predicted onset locations for finer meshes. In contrast, the crossflow model shows a slower convergence rate, indicating greater sensitivity to grid resolution. This indicates that the crossflow model requires a more refined grid than the streamwise model to achieve a grid independent solution. Nevertheless, as shown in the figure, monotonic convergence is still achieved. The increased sensitivity can be attributed to the crossflow transition criteria, as all other aspects of both models remain identical. Finally, based on the grid independence study, the *Finer* grid was selected for the remaining analysis.

3.1.2. ***Study of the Swept Wing at Multiple Reynolds Numbers.*** Figure 4 illustrates the transition onset location predicted by both the streamwise and crossflow models at three different Reynolds numbers. The transition location for each case was chosen as the point that saw the largest change in the skin-friction coefficient distribution over the suction side. Notably, the streamwise model consistently predicts a transition location that remains relatively unchanged across varying Reynolds numbers, thus failing to accurately capture the true onset location, especially at high Reynolds numbers. Conversely, the crossflow model demonstrates the ability to replicate the trend observed in experimental data with good accuracy.

Figure 5 shows the distribution of skin-friction coefficient on the swept wing surface along with limiting streamlines at different Reynolds numbers. The left column shows the predictions made by the streamwise transition model while the right column shows the crossflow model predictions. From experimental observations for the swept wing, it is known that at the lowest Reynolds number, transition is triggered

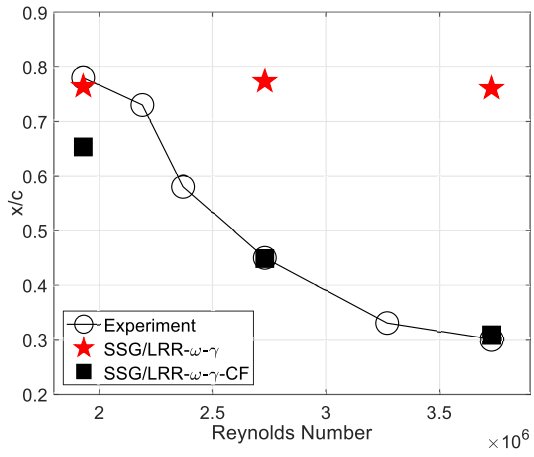

Figure 4. Predicted transition onset on the suction side at different Reynolds numbers

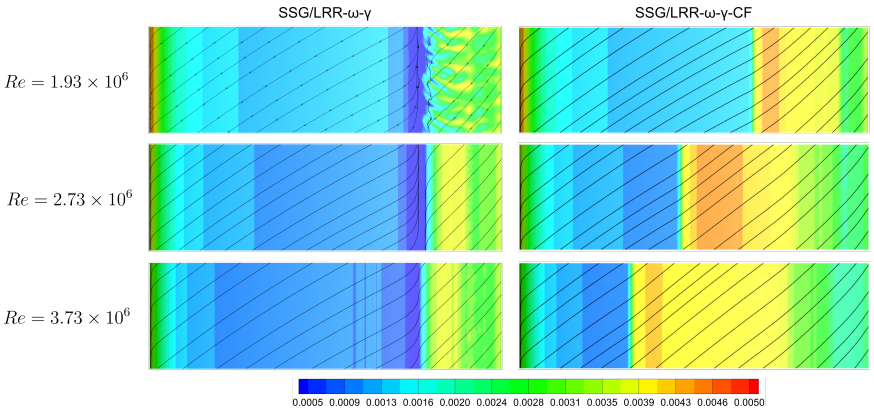

Figure 5. C_f contour at different Reynolds numbers with surface streamlines on the suction side

predominantly by laminar separation and as the Reynolds number increases, crossflow transition becomes more prominent [3,28]. In Fig. 5, at the lowest Reynolds number the streamwise model predicts transition initiated by laminar separation, consistent with experimental measurements, and corroborated by Fig. 4. The crossflow model does not predict any laminar separation, instead predicts crossflow transition slightly upstream. As Reynolds number increases, the streamwise model continues to predict separation-induced transition (or natural transition at the highest Reynolds number), while the crossflow model successfully captures crossflow-instability induced transition. As a result, the crossflow model also predicts a much higher skin-friction coefficient along the wing surface, while the streamwise model predicts a largely laminar flow with low levels of skin-friction. In summary, the superior accuracy of the SSG/LRR-ω-γ-CF model highlights the importance of incorporating crossflow transition models.

3.2. **DLR 6:1 Prolate Spheroid.** The DLR 6:1 prolate spheroid is a good test case to validate the current model, since it manifests complex 3-D flows involving crossflow transition and free-wake vortices. The flow around the spheroid is subject to pressure gradients in the stream-wise as well as the span-wise directions , similar to the flow observed on any underwater vehicle of a general 'drag-optimized' shape. Experimental data on the spheroid is taken from the tests that were carried out at the DLR Göttingen 3x3 low-speed wind tunnel in 1980 as reported in [24]. In the current study the spheroid is analyzed at three angles of attack (α) and a Reynolds number of 6.5×10^6.

Figure 6 shows the grid for the case where $\alpha = 10^o$, with the zoomed in window highlighting the surface and the near-wall grid. The computational domain has a cross-section of $3m \times 3m$, in agreement with the cross-section of the tunnel test section. All domain walls were assigned a slip wall boundary condition, whereas the spheroid surface was set to a no-slip wall boundary condition. The free-stream velocity was set to 45 m/s. The turbulence intensity at the inlet, located 3 m upstream of the spheroid's leading edge, was set to 0.3%. This value was chosen to ensure it decays to 0.15% at the leading edge,

aligning with the experimental conditions specified by Kreplin *et al.* [24]. The viscosity ratio at the inlet (ν_t/ν) is set to a value of 2.

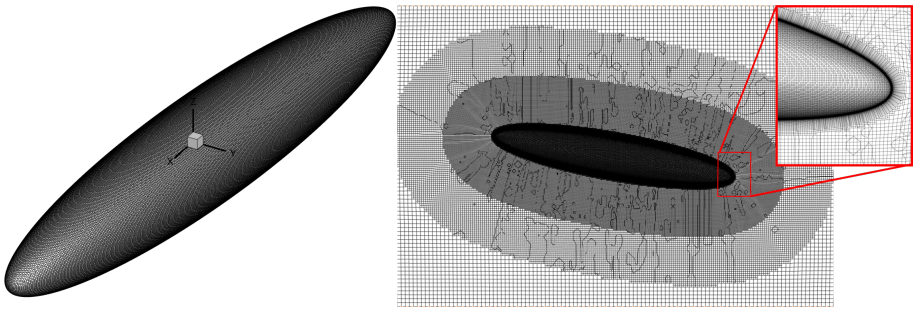

Figure 6. Near-body grid for the DLR 6:1 prolate spheroid

3.2.1. ***Grid Independence Study.*** The grid independence study for the spheroid was conducted using four different grids at a free-stream Reynolds number of 6.5×10^6 and an angle of attack, $\alpha = 10°$. As with the previous test case, parameters affecting near-wall and surface resolution were prioritized and are outlined in Table 2.

Table 2. Mesh Parameters for grid-independence study on the DLR 6:1 Prolate Spheroid at Re $= 6.5 \times 10^6$ and $\alpha = 10°$

	Coarse	**Medium**	**Fine**	**Very Fine**
Δx_{body}	0.0125 m	0.0075 m	0.005 m	0.0037 m
$y^+(1)$	1.2	1	0.8	0.6
Prism Layers	35	45	65	80
Total resolution	946,766	3,774,781	12,294,680	28,159,365

Figure 7 shows the contours of skin-friction coefficient predicted by the crossflow model. Sectional markers (in black) have been shown to aid in better visualization of the contour and transition locations. For reference, the experimental contour from Nie *et al.* [18] is included. The predicted contours are color-matched to the experimental data, except that the white in the experimental contour corresponds to light green in the predicted results. It is seen that the crossflow transition is captured by all grids. The transition location, specifically in the mid-portion of the body, tends to move downstream with an increase in resolution. On the windward side, however, the model predicts a reduced extent of the turbulent region as the resolution increases. The prediction made by the *Coarse* mesh along the windward side is seen to align closest with the experimental data. A similar effect is also observed in the helicity-based SSG/LRR-ω-γ-Re$_{\theta t}$ crossflow transition model proposed by Nie *et al.* [18]. Further, Fig. 8 shows the skin-friction coefficient distribution along the spheroid's centerline, predicted by various grids. Very good grid convergence is observed for the model along this section. It can be concluded that the transition observed on the windward side is significantly more sensitive to mesh resolution compared to the transition on the leeward side and the mid-body. Based on these observations, the *Fine* mesh resolution has been chosen for the remaining analyses. The simulation setup, including the numerical scheme and solver settings, were consistent with that used for the swept wing.

3.2.2. ***Spheroid at*** $\alpha = 5^o$. Figure 9 shows the distribution of skin-friction coefficient predicted by the streamwise and crossflow transition models at $\alpha = 5^o$. These predictions have also been compared against the fully turbulent model predictions. It is evident that the fully turbulent model predicts a largely different flow contour compared to reality. On the other hand, at the current angle of attack, both streamwise and crossflow transition models exhibit very similar behavior. Figure 10 demonstrates that both the streamwise and crossflow models predict the transition onset reasonably well, with the crossflow model showing slightly better accuracy. However, the streamline model tends to show better prediction accuracy in the regions below the spheroid centerline.

From previous works [29], it was shown that the spheroid experiences transition initiated by simultaneous excitation of Tollmein-Schlichting (TS) and crossflow instabilities, resulting in a mix of natural and crossflow transition at this test condition. This makes the case highly complex to model. It was explained that the windward side sees transition triggered by TS-waves. Both transition models seem to be able

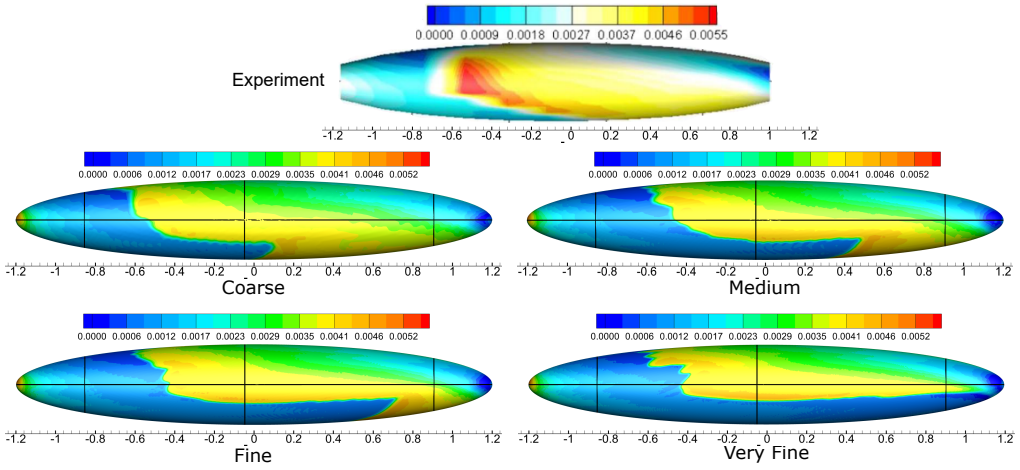

Figure 7. C_f distribution predicted by SSG/LRR-ω-γ-CF. Grid independence study performed at $\alpha = 10^o$ and Re$= 6.5 \times 10^6$. Experimental contour from [18].

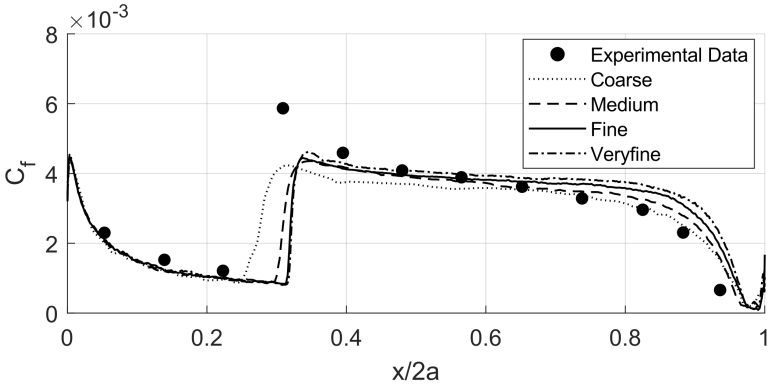

Figure 8. C_f predicted by different meshes along the X-Z plane of the spheroid at an angle of attack, $\alpha = 10°$

to capture this effect, albeit with slightly better accuracy observed in the streamwise model. This could imply that the coupling of the streamwise and crossflow transition production terms could be modified to improve the state of the crossflow transition model in predicting natural transition. It is important to note that even at the finer mesh resolutions, the current transition model tends to predict the transition at the windward side, which has not been observed in any other crossflow model. Furthermore, the overall similarity of the streamwise model to the crossflow model is very specific to the current formulation and has not been observed in any other transition model.

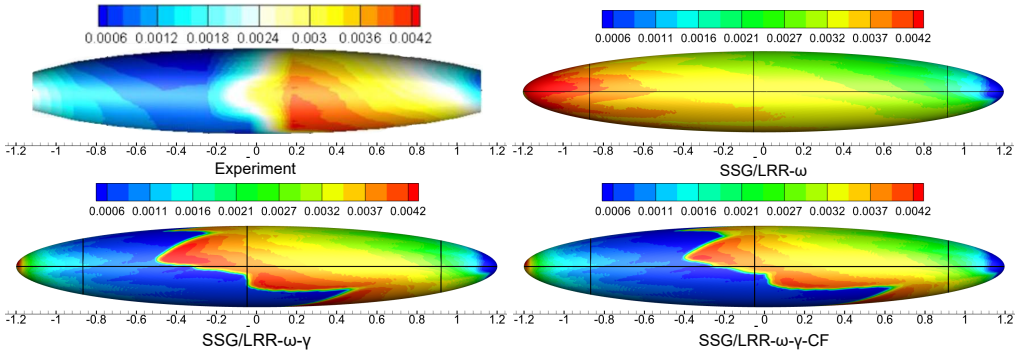

Figure 9. C_f contour at $\alpha = 5^o$ and Re$=6.5 \times 10^6$. Experimental contour from [18].

3.2.3. ***Spheroid at*** $\alpha = 10^o$. The skin-friction distribution at the test condition of $\alpha = 10^o$ is shown in Fig. 11. A separation region is observed near the leeward side, close to the trailing edge, and is highlighted

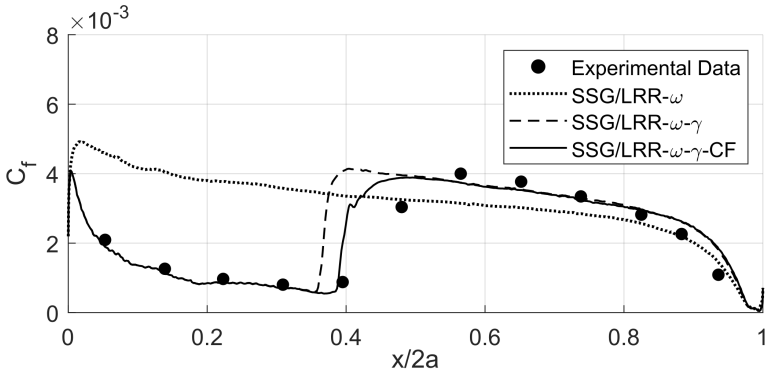

Figure 10. C_f along the X-Z cutting plane at $\alpha = 5°$ and Re=6.5×10^6

using red dotted lines. This region was identified based on experimental streamlines reported by Kreplin *et al.* [24] and further supported by the findings of Pisharoti *et al.* [23]. In strongly three-dimensional flows, such separation is typically indicated by converging streamlines and a significant reduction in the skin-friction coefficient. All models capture this separation region, which is approximately delineated in the figure with red dotted lines and light blue contour. It should be noted that the red dotted lines are approximate and do not represent the exact separation line. They are included solely to help highlight the light-blue contour region, which corresponds to the area of flow separation. SSG/LRR-ω-γ-CF is able to capture the onset of crossflow transition along the leeward and mid-portion of the body with good accuracy. It was shown that even at $\alpha = 10^o$, there is transition initiated by TS-waves [29]. The streamwise transition model predicts transition onset on the leeward side and also manages to predict better transition at the windward side. However, it predicts laminar flow along most of the mid portion of the body. Figure 12 further reinforces that fact that the crossflow model is able to accurately predict crossflow transition onset along the xz-plane, outperforming the streamwise model in regions where crossflow instability is dominant.

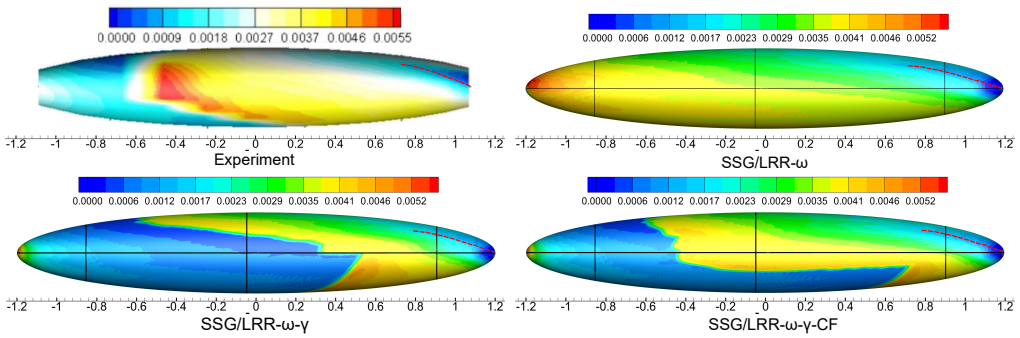

Figure 11. C_f contour at $\alpha = 10^o$ and Re=6.5×10^6. Experimental contour from [18].

3.2.4. ***Spheroid at*** $\alpha = 20^o$. At this high inclination, the flow experiences pure crossflow transition. Figure 13 shows that the spheroid experiences separation starting from the leeward side (at $x \approx -0.4m$) all the way to the trailing edge and is indicated by the light-blue region in the experimental contour. This separation is well captured by both the fully turbulent and crossflow transition models. In contrast, the streamwise transition model under-predicts the extent of separation, as seen from the smaller blue region and the red dotted line marking the approximate separation line in each contour. The streamwise transition model predicts transition onset on the leeward side but fails to capture transition along the mid-portion and windward side of the body. In contrast, the crossflow model successfully captures the onset of crossflow transition and provides a good approximation of the transition pattern and turbulent region along the entire body, as also illustrated in Fig. 14.

4. Conclusion

This paper presents the principal characteristics of a Reynolds stress transport based transitional model, SSG/LRR-ω-γ, that has been extended to include crossflow induced turbulence transition. The

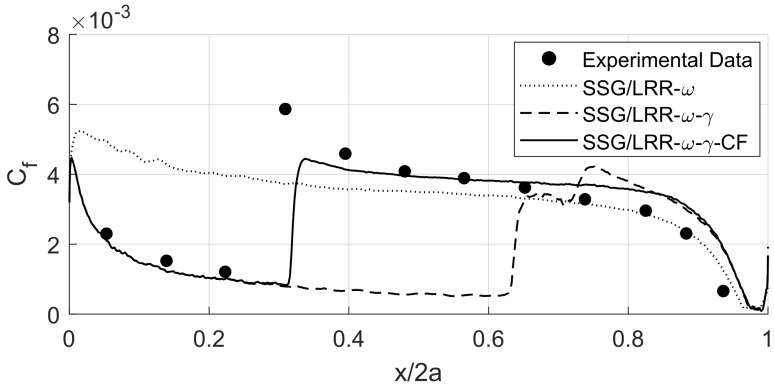

Figure 12. C_f along the X-Z cutting plane at $\alpha = 10°$ and Re=6.5×10^6

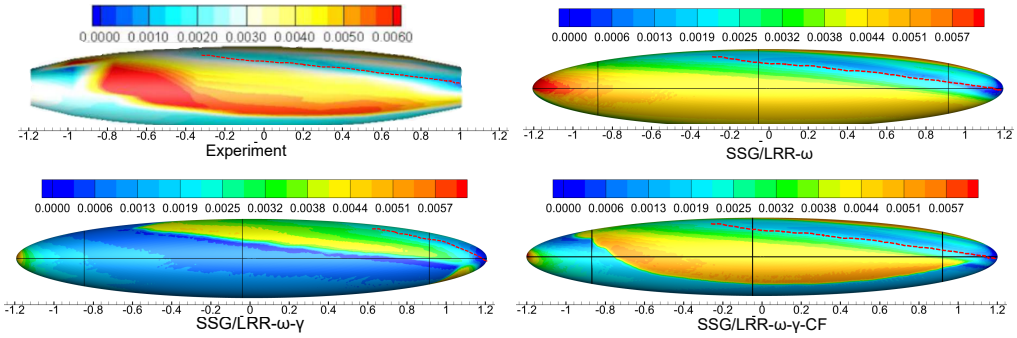

Figure 13. C_f contour at $\alpha = 20^o$ and Re=6.5×10^6. Experimental contour from [18].

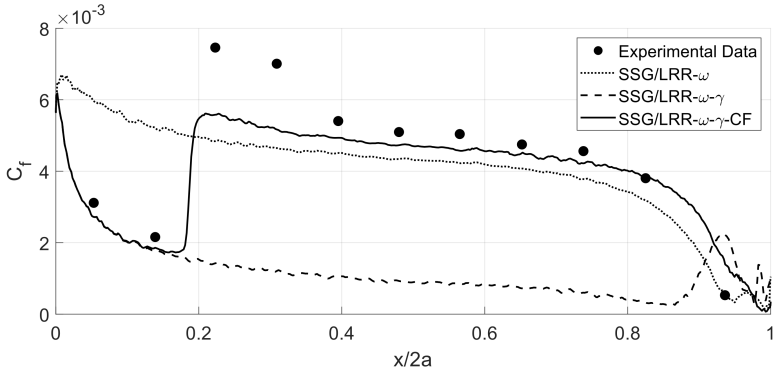

Figure 14. C_f along the X-Z cutting plane at $\alpha = 20°$ and Re=6.5×10^6

modification to the original streamwise transition model formulation was made by adding a term to the intermittency production that accounts for crossflow transition. This additional term utilizes a local helicity-based formulation, as helicity has been identified as a significant contributor to the crossflow velocity gradient and is used to capture crossflow instabilities. The addition of the crossflow term however, makes the current model lose its ability to be Galilean invariant.

The novel crossflow model was validated using two test cases; the NLF (2)-0415 infinite swept wing and the DLR 6:1 prolate spheroid. A grid sensitivity study was conducted for both cases, revealing that the crossflow model exhibited slower grid convergence than the streamwise model, necessitating a refined mesh for accurate transition prediction.

For the swept wing, the model was tested across different Reynolds numbers, demonstrating superior accuracy in predicting transition onset compared to the streamwise model. For the spheroid, the model was evaluated at various inclinations, successfully capturing crossflow transition with good accuracy. The streamwise model consistently failed to capture the correct transition mechanism, frequently predicting largely laminar flow profiles in cases dominated by crossflow instabilities. In regions where streamwise

transition was dominant along the spheroid, typically at lower inclinations, the crossflow model exhibited slightly lower accuracy than the streamwise model.

In conclusion, the current work has established a simple, yet efficient transition turbulence model framework that has been implemented on OpenFOAM. The turbulence model libraries pertaining to the original streamwise model and its crossflow extension is made available on GitHub for the OpenFOAM community.

Acknowledgements

The authors would like to thank Jack Webster for his preliminary work on the transition model, which helped lay the foundation for the proposed model. The authors would also like to acknowledge the Advanced Research Computing at Virginia Tech for providing computational resources that have contributed to the results reported within this paper. URL: http://www.arc.vt.edu

Author Contributions: Conceptualisation, N.P and S.B; Methodology, software, validation and investigstion, N.P. ; supervision, resources, project administration, funding acquisition, S.B.; writing—original draft preparation, N.P.; writing—review and editing, N.P. and S.B.; All authors have read and agreed to the published version of the manuscript.

References

[1] L. Xu, E. Baglietto, and S. Brizzolara, "Extending the applicability of rans turbulence closures to the simulation of transitional flow around hydrofoils at low reynolds number," *Ocean Engineering*, vol. 164, pp. 1–12, 2018.

[2] L. M. Miller, T. Njaka, S. Brizzolara, and T. Curtin, "Drag reduction and power optimization due to an innovative, toroidal hull form of an auv," in *IOP Conference Series: Materials Science and Engineering*, vol. 1288, no. 1. IOP Publishing, 2023, p. 012039.

[3] J. Dagenhart and W. S. Saric, "Crossflow stability and transition experiments in swept-wing flow," Tech. Rep., 1999.

[4] N. Beck, T. Landa, A. Seitz, L. Boermans, Y. Liu, and R. Radespiel, "Drag reduction by laminar flow control," *Energies*, vol. 11, no. 1, p. 252, 2018.

[5] S. Pawar and S. Brizzolara, "Relevance of transition turbulent model for hydrodynamic characteristics of low reynolds number propeller," *Applied Ocean Research*, vol. 87, pp. 165–178, 2019.

[6] N. Pisharoti and S. Brizzolara, "Validation study of reynolds stress model coupled with gamma transition for uav propellers," in *ASME International Mechanical Engineering Congress and Exposition*, vol. Volume 10: Fluids Engineering, 2021.

[7] N. Pisharoti, J. Whelchel, W. N. Alexander, and S. Brizzolara, "Cfd-based aerodynamic and aeroacoustic analysis of large payload multi-copter rotors," in *AIAA SCITECH 2023 Forum*, 2023, p. 0617.

[8] R. E. Mayle, "The 1991 IGTI Scholar Lecture: The Role of Laminar-Turbulent Transition in Gas Turbine Engines," *Journal of Turbomachinery*, vol. 113, no. 4, pp. 509–536, 10 1991.

[9] F. Menter, "A correlation-based transition model using local variables - part i: Model formulation," pp. 413–422, 2006.

[10] F. R. Menter, P. E. Smirnov, T. Liu, and R. Avancha, "A one-equation local correlation-based transition model," *Flow, Turbulence and Combustion*, vol. 95, pp. 583–619, 2015.

[11] S. Nie, N. Krimmelbein, A. Krumbein, and C. Grabe, "Coupling of a reynolds stress model with the γ-re$_{\theta t}$ transition model," *AIAA Journal*, vol. 56, no. 1, pp. 146–157, 2018.

[12] N. Pisharoti, J. Webster, and S. Brizzolara, "Reynolds stress turbulence modelling with γ transition model," *International Journal of Computational Fluid Dynamics*, vol. 36, no. 1, pp. 21–43, 2022.

[13] C. Grabe and A. Krumbein, "Correlation-based transition transport modeling for three-dimensional aerodynamic configurations," *Journal of Aircraft*, vol. 50, no. 5, pp. 1533–1539, 2013.

[14] S. Medida and J. Baeder, "A new crossflow transition onset criterion for rans turbulence models," in *21st AIAA Computational Fluid Dynamics Conference*, 2013, p. 3081.

[15] R. Langtry, "Extending the gamma-rethetat correlation based transition model for crossflow effects," in *45th AIAA fluid dynamics conference*, 2015, p. 2474.

[16] C. Grabe, N. Shengyang, and A. Krumbein, "Transition transport modeling for the prediction of crossflow transition," in *34th AIAA applied aerodynamics conference*, 2016, p. 3572.

[17] S. Vallinayagam Pillai and S. Lardeau, "Accounting crossflow effects in one-equation local correlation-based transition model," in *8th AIAA Theoretical Fluid Mechanics Conference*, 2017, p. 3159.

[18] S. Nie, N. Krimmelbein, A. Krumbein, and C. Grabe, "Extension of a reynolds-stress-based transition transport model for crossflow transition," *Journal of Aircraft*, vol. 55, no. 4, pp. 1641–1654, 2018.

[19] G. Schubauer and H.K.Skramstad, "Laminar boundary-layer oscillations and stability of laminar flow," *Journal Of The Aeronautical Sciences*, vol. 14, no. 2, pp. 69–78, 1947.

[20] C. Müller and F. Herbst, "Modelling of crossflow-induced transition based on local variables," *Proc. ECCOMAS, Paper*, no. 2252, p. 72, 2014.

[21] D. Arnal, M. Habiballah, and E. Coustols, "Théorie de l'instabilité laminaire et critères de transition en écoulement bi et tridimensionnel," *La Recherche Aérospatiale*, no. 2, pp. 125–143, 1984.

[22] Y. S. Jung and J. Baeder, "$\gamma - re_{\theta t}$ spalart-allmaras with crossflow transition model using hamiltonian-strand approach," *Journal of Aircraft*, vol. 56, no. 3, pp. 1040–1055, 2019.

[23] N. Pisharoti, L. Miller, and S. Brizzolara, "Comparative study of first and second-order closure rans transition turbulence models for the 6:1 prolate spheroid," in *34th Symposium on Naval Hydrodynamics*, 2022.

[24] H. Kreplin, H. Vollmers, and H. Meier, "Wall shear stress measurements on an inclined prolate spheroid in the dfvlr 3 m× 3 m low speed wind tunnel, goettingen," *DFVLR-AVA, Report IB*, pp. 22–84, 1985.

[25] B. Eisfeld, C. Rumsey, and V. Togiti, "Verification and validation of a second-moment-closure model," *AIAA Journal*, vol. 54, no. 5, pp. 1524–1541, 2016.
[26] J. Cliquet, R. Houdeville, and D. Arnal, "Application of laminar-turbulent transition criteria in navier-stokes computations," *AIAA Journal*, vol. 46, no. 5, pp. 1182–1190, 2008.
[27] C. Rumsey, "Ssg/lrr full reynolds stress model," *URL https://turbmodels.larc.nasa.gov/rsm-ssglrr.html*, 2017.
[28] J. H. Choi and O. J. Kwon, "Enhancement of a correlation-based transition turbulence model for simulating crossflow instability," *AIAA Journal*, vol. 53, no. 10, pp. 3063–3072, 2015.
[29] N. Krimmelbein and R. Radespiel, "Transition prediction for three-dimensional flows using parallel computation," *Computers & Fluids*, vol. 38, no. 1, pp. 121–136, 2009.
[30] F. R. Menter, "Two-equation eddy-viscosity turbulence models for engineering applications," *AIAA journal*, vol. 32, no. 8, pp. 1598–1605, 1994.

Appendix A. Complete Formulation of the Streamwise Transition Model: SSG/LRR-ω-γ

The transport equation for the Reynolds stress tensor in the SSG/LRR-ω model is given by

$$\frac{\partial \rho R_{ij}}{\partial t} + \frac{\partial (\rho U_k R_{ij})}{\partial x_k} = \rho P_{ij} + \rho \Pi_{ij} - \rho \epsilon_{ij} + \rho D_{ij}, \tag{23}$$

where $R_{ij} = u_i u_j$ represents the Cartesian components of the Reynolds stress tensor, ρ is the density, and μ is the dynamic viscosity of the fluid. The model correlations and constants for this transport equation are unchanged from the formulation presented by Eisfeld textitet al. [25]. The Reynolds stress production term P_{ij} is given by

$$\rho P_{ij} = -\rho R_{ik} \frac{\partial U_j}{\partial x_k} - \rho R_{jk} \frac{\partial U_i}{\partial x_k}. \tag{24}$$

There is no modeling required for this term, as information regarding velocity gradient and Reynolds stress tensor is available from the system of equations and thereby gives the exact value. The remaining three terms in the Reynolds stress transport equation, ϵ_{ij}, D_{ij} and Π_{ij}, are modeled based on mathematical relations which hold true for both SSG and LRR models. The dissipation, ϵ_{ij}, and the isotropic dissipation rate, ϵ, are given by

$$\rho \epsilon_{ij} = \frac{2}{3} \rho \epsilon \delta_{ij}; \quad \epsilon = C_\mu k \omega, \tag{25}$$

where $C_\mu = 0.09$ and $k = R_{ii}/2$ is the kinetic energy. A transport equation for the specific dissipation rate k is shown later. The diffusion of the Reynolds stress tensor, D_{ij}, is modeled using generalized gradient diffusion (GGD) and is given by

$$\rho D_{ij} = \frac{\partial}{\partial x_k} \left[\left(\mu \delta_{kl} + D^{(GD)} \frac{\rho R_{kl}}{C_\mu \omega} \right) \frac{\partial R_{ij}}{\partial x_l} \right]. \tag{26}$$

The pressure strain term , Π_{ij}, which is specific to the Reynolds stress transport equation, is applied to redistribute the turbulent stresses. It is given by

$$\begin{aligned} \rho \Pi_{ij} = &- \left(C_1 \rho \epsilon + \frac{1}{2} C_1^* \rho P_{kk} \right) b_{ij} + C_2 \rho \epsilon \left(b_{ik} b_{kj} - \frac{1}{3} b_{kl} b_{kl} \delta_{ij} \right) + \left(C_3 - C_3^* \sqrt{b_{kl} b_{kl}} \right) \rho k S_{ij}^* \\ &+ C_4 \rho k \left(b_{ik} S_{jk} + b_{jk} S_{ik} - \frac{2}{3} b_{kl} S_{kl} \delta_{ij} \right) + C_5 \rho k \left(b_{ik} W_{jk} + b_{jk} W_{ik} \right), \end{aligned} \tag{27}$$

where, b_{ij}, S_{ij} and W_{ij} are Cartesian components of the anisotropic tensor, the mean strain rate tensor and the vorticity tensor, respectively, while S_{ij}^* is the deviatoric component of the mean strain rate tensor, as

$$b_{ij} = \frac{R_{ij}}{2k} - \frac{1}{3}\delta_{ij}, \quad S_{ij} = \frac{1}{2}\left(\frac{\partial U_i}{\partial x_j} + \frac{\partial U_j}{\partial x_i} \right), \quad S_{ij}^* = S_{ij} - \frac{1}{3} S_{kk} \delta_{ij}, \quad W_{ij} = \frac{1}{2}\left(\frac{\partial U_i}{\partial x_j} - \frac{\partial U_j}{\partial x_i} \right). \tag{28}$$

The constants C_{1-5} are the same as given by Eisfeld textitet al. [25]. P_{kk} is the trace of the production term, P_{ij}.

The specific dissipation transport equation, also known as length scale determining equation, is given by

$$\frac{\partial (\rho \omega)}{\partial t} + \frac{\partial (\rho U_k \omega)}{\partial x_k} = \frac{\alpha_\omega \omega}{k} \frac{\rho P_{kk}}{2} - \beta_\omega \rho \omega^2 + \frac{\partial}{\partial x_k} \left[\left(\mu + \sigma_\omega \frac{\rho k}{\omega} \right) \frac{\partial \omega}{\partial x_k} \right] + \sigma_d \frac{\rho}{\omega} max \left(\frac{\partial k}{\partial x_j} \frac{\partial \omega}{\partial x_j}, 0 \right), \tag{29}$$

including the production term which is a function of the trace of the Reynolds stress production, the dissipation, diffusion and cross-diffusion terms. Here, α_ω, β_ω, σ_ω and σ_d are blended using Menter's SST blending function, F_1, [30] and are calculated as

$$\phi = F_1 \phi_{LRR} + (1 - F_1) \phi_{SSG}, \tag{30}$$

where, ϕ_{LRR} represents the LRR model coefficients which are applied in the near wall regions ($F_1 = 1$) and ϕ_{SSG} represents the SSG model coefficients which are applied beyond the edge of the boundary layer ($F_1 = 0$). The blending function is given by

$$F_1 = tanh(\zeta^4), \tag{31}$$

where the argument ζ is defined as

$$\zeta = \min \left[\max \left(\frac{\sqrt{\tilde{k}}}{C_\mu \omega d}, \frac{500\mu}{\rho \omega d^2} \right), \frac{4 \sigma_\omega^{SSG} \rho \tilde{k}}{\sigma_d^{SSG} \frac{\rho}{\omega} \max \left(\frac{\partial \tilde{k}}{\partial x_k} \frac{\partial \omega}{\partial x_k}, 0 \right) d^2} \right]. \tag{32}$$

The values of the model constants are given in Tabs. 3 and 4.

Table 3. ω-transport equation model constants

	α_ω	β_ω	σ_ω	σ_d
SSG	0.44	0.083	0.856	1.712
LRR	0.56	0.075	0.5	0

Table 4. Reynolds Stress transport equation model constants

	C_1	C_1^*	C_2	C_3	C_3^*	C_4	C_5	$D^{(GD)}$
SSG	3.4	1.8	4.2	0.8	1.3	1..25	0.4	0.22
LRR	3.6	0	0	0.8	0	$\frac{18C_2^{LRR}+12}{11}$	$\frac{-14C_2^{LRR}+20}{11}$	0.75 C_μ

A.1. γ **Transition Model.** The γ transition model [10] is governed by the intermittency transport equation, given by

$$\frac{\partial(\rho\gamma)}{\partial t} + \frac{\partial(\rho U_j\gamma)}{\partial x_j} = P_\gamma - E_\gamma + \frac{\partial}{\partial x_j}\left[\left(\mu + \frac{\mu_t}{\sigma_\gamma}\right)\frac{\partial\gamma}{\partial x_j}\right], \tag{33}$$

where σ_γ is a model constant equal to 1. All the model correlations and constants for this transport equation are taken from the one-equation transition model formulation presented by Menter et al [10]. The source term for transition is defined as

$$P_\gamma = F_{length}\rho S\gamma(1-\gamma)F_{onset}, \tag{34}$$

where F_{length} is used to control the magnitude of the production term and is set to 100. The term S is the magnitude of the strain rate and '$(1-\gamma)$' is used to limit the value of intermittency to 1. This is done to ensure that intermittency does not exceed the freestream value, which is set to 1 [9]. F_{onset} is an important term that is responsible for triggering the transition mechanism which in turn indicates the onset of intermittency production. It is set off when the vorticity Reynolds number exceeds the set transition criteria given in

$$\begin{gathered} F_{onset1} = \frac{Re_\nu}{2.2Re_{\theta c}}, \quad F_{onset2} = min(F_{onset1}, 2.0), \\ F_{onset3} = max\left(1 - \left(\frac{R_T}{3.5}\right)^3, 0\right), \quad F_{onset} = max(F_{onset2} - F_{onset3}, 0), \end{gathered} \tag{35}$$

where $Re_\nu = \frac{\rho y^2 S}{\mu}$ is the vorticity Reynolds number and R_T is the viscosity ratio ($R_T = \frac{\rho k}{\mu\omega}$). The term $Re_{\theta c}$ is the critical Reynolds number and is the point where the intermittency begins to rise and turbulence begins to grow. The correlation for $Re_{\theta c}$ is taken from Menter textitet al. [10].

The dissipation term, E_γ, ensures that the intermittency stays close to zero in the laminar boundary layer regions and is given by

$$E_\gamma = c_{a2}\rho\Omega\gamma F_{turb}(c_{e2}\gamma - 1). \tag{36}$$

Model constants c_{a2} and c_{e2} are equal to 0.06 and 50, respectively. Ω is the absolute vorticity magnitude. F_{turb} is responsible to turn off dissipation in turbulent regions and in the viscous sublayer and it is given by

$$F_{turb} = e^{-\left(\frac{R_T}{2}\right)^4}. \tag{37}$$

The γ transition model includes a modification to the original blending function (F_{1orig}) introduced by Menter textitet al. [9,30], given by

$$R_y = \frac{\rho y\sqrt{k}}{\mu} \quad , \quad F_3 = e^{-\left(\frac{R_y}{120}\right)^8} \quad , \quad F_1 = \max(F_{1orig.}, F_3), \tag{38}$$

which consistently sets the value of F_1 equal to 1 in the laminar region. This is to ensure that the near wall LRR turbulence model remains active in laminar, transition and turbulent regions in the boundary layer.

The Reynolds stress model, SSG/LRR-ω, and the intermittency transport equation, γ, are coupled by scaling the production, dissipation and pressure strain terms of the Reynolds stress transport equation with γ as in

$$\tilde{P}_{ij} = \gamma P_{ij} \quad , \quad \tilde{\Pi}_{ij} = \gamma\Pi_{ij} \quad , \quad \tilde{\epsilon}_{ij} = \max(\gamma, 0.1)\epsilon_{ij}. \tag{39}$$

A.2. **Modifications to the SSG/LRR-ω-γ Model.** This subsection reiterates content presented earlier in Section 2.1, and is included here to present the complete model formulation in a self-contained manner.

In RST-based transition models, as the Reynolds stress tensor (R_{ij}) goes down to near zero values in the fully laminar regions, the turbulence production term becomes negligible. Since the production of the specific dissipation rate is directly proportional to the trace of turbulence production (P_{kk}), as

$$P_{\omega_{RST}} = \frac{\alpha_\omega \omega}{k} \frac{\rho P_{kk}}{2}, \tag{40}$$

the dissipation also drops to really low levels. This reduction leads to a faster turbulence growth rate and premature transition. However, this issue does not arise in SST-based transition models, where the dissipation terms are a function of the mean strain rate (S), as

$$P_{\omega_{SST}} = \frac{\alpha_\omega}{\nu_t} \left(-\rho R_{ik} \frac{\partial U_i}{\partial x_k} \right) = \alpha_\omega \rho S^2, \tag{41}$$

which stems directly from the Boussinesq approximation $R_{ij} = -\ (\ 2\nu_t S_{ij} - 2k\delta_{ij}/3\ )$, where ν_T is the turbulent kinematic viscosity.

Therefore, a modification was introduced to the dissipation production as

$$\tilde{P}_\omega \ = \ (1 \ - \ C_{lam}) P_{\omega_{SST}} \ + \ C_{lam} P_{\omega_{RST}}, \tag{42}$$

where

$$C_{lam} \ = \ \begin{cases} 0 & \text{if } c_\omega \ > \ \gamma \\ \frac{\gamma - c_\omega}{1 - c_\omega} & \text{if } c_\omega \ < \ \gamma \end{cases} \text{ and } c_\omega \ = \ \left(\exp\left(- \left(\frac{420}{Re_{\theta c} + C_{Re}} \right)^4 \right) \right)^2, \tag{43}$$

$$C_{Re} = 500.$$

Here, C_{lam} is a blending function that equals 0 in laminar regions which activates the SST-based formulation of dissipation production and equals 1 in turbulent regions, which activates the original formulation of RST-based dissipation production. The term C_{Re} is a model constant and is accessible to the user for any changes. The term $Re_{\theta c}$ represents the critical Reynolds number and is a key parameter in defining the streamwise transition criteria. This modified hybrid formulation helps in predicting transition for cases with high free-stream turbulence by improving ω prediction in fully laminar regions.

Additionally, in cases with low levels of free-stream turbulence, it has been observed that the SSG/LRR-ω-γ model takes longer to generate turbulence within the boundary layer, even though the transition is triggered at the correct location [10, 12]. Therefore, an auxiliary turbulence production term, P_{ij}^{lim} was introduced and added to the original Reynolds stress production, as

$$\tilde{P}_{ij} = \gamma P_{ij} + P_{ij}^{lim}, \tag{44}$$

where

$$P_{ij}^{lim} = 5 C_k max(\gamma - 0.2, 0)(1 - \gamma) F_{on}^{lim} max(3 C_{SEP} \nu - \nu_T, 0) \frac{\omega}{k} P_{kk} \delta_{ij}. \tag{45}$$

It aids in generating additional turbulence when transition is driven by laminar separation, or by TS wave growth. The term is activated when transition is triggered and deactivated once the flow becomes fully turbulent. The onset term F_{on}^{lim} is given by

$$F_{lim}^{on} = \min\left(\max\left(\frac{Re_\nu}{2.2 Re_{\theta_C}^{lim}} - 1, 0 \right), 3 \right) \quad , \quad Re_{\theta_c}^{lim} = 1100. \tag{46}$$

The constant C_k controls the magnitude of supplementary turbulence production and is equal to 1. The constant C_{SEP}, which is set to 1, is responsible to deactivate the supplementary term when the magnitude of turbulent viscosity (ν_T) goes higher than three times the kinematic viscosity (ν). The term $Re_\nu = \frac{\rho y^2 S}{\mu}$ stands for vorticity Reynolds number, where S is the magnitude of the mean strain rate tensor and y is the distance from the wall.